United Kingdom Atomic Energy Authority

UKAEA FUS 525

R. Pampin

Tungsten transmutation and resonance self-shielding in PPCS models for the study of sigma-phase formation

Tungsten transmutation and resonance self-shielding in PPCS models for the study of sigma-phase formation

R. Pampin

EURATOM/UKAEA Fusion Association, Culham Science Centre, OX14 3DB, Abingdon, UK

UKAEA FUS 525

EURATOM/UKAEA Fusion

Tungsten transmutation and resonance self-shielding in PPCS models for the study of sigma-phase formation

R. Pampin

October 2005

EURATOM/UKAEA Fusion Association

Culham Science Centre
Abingdon
Oxfordshire
OX14 3DB
United Kingdom

Telephone: +44 1235 820220
Facsimile: +44 1235 466435

UKAEA Fusion Working in Europe

Abstract

Transmutation reactions in plasma-facing tungsten produce rhenium and osmium at levels which may trigger the formation of brittle sigma phase in the W-Re-Os alloy. A study has been carried out, updating previous work, to analyse this issue in three fusion power plant models whose neutron transport behaviour is representative of a wide range of possible options. Self-shielding effects in giant tungsten resonances have now been accounted for. Results show the importance of this treatment and the significant influence of the overall neutron behaviour in the blanket, in particular the presence of strongly moderating materials such as water or beryllium. Analysis of the evolution of the Re/Os concentrations with time shows that in no case is sigma phase formation potential reached within the service lifetime of the components.

Tungsten transmutation and resonance self-shielding in PPCS models

1. Introduction

Neutron irradiation produces transmutation of all materials surrounding the plasma, altering its original composition and giving rise to issues related to the activity and characteristics of the transmutation products. As part of the European Power Plant Conceptual Study (PPCS), [1], safety and environmental implications of material transmutation were assessed in a range of power plant concepts exploring a wide spectrum of conceivable options for future electricity production using tokamak burning plasmas. The case of tungsten armours was later studied with particular detail, due to their potentially important impact in operational and public safety, [2].

Another important issue associated with transmutation is that it may alter the performance of plasma-facing (PF) components, i.e. armours and divertor target plates, commonly very sensitive to changes in material properties due to the extremely demanding conditions they must withstand. Tungsten is a candidate for these components due to its high melting point and resilience to sputtering by ions. Transmutation of tungsten under typical D-T fusion neutron spectra leads mainly to the formation of rhenium and osmium isotopes, as well as small traces of other elements. The mechanical stability of W-Re-Os alloys is very different to that of pure tungsten: irradiation-induced hardening and embrittlement due to the formation of σ and χ phase precipitates have been reported, [3,4]. Transmutation of tungsten during its service life in a fusion power plant might thus result in a severe challenge to the integrity of the armour and divertor plates where it is used, [5].

In order to assess the onset of this effect, analyses have been performed of the compositional changes of tungsten under typical fusion power plant plasma-facing conditions. Previous calculations have been updated, and the level of detail increased, in order to account for the following issues:

i. Self-shielding effects of giant resonances in the overall transmutation of tungsten, not taken into account before but thought to be very important for the accurate calculation of transmutation product levels; these effects and levels are greatly dependent on the energy and spatial treatments of the inventory codes and geometry modelling used during the transmutation analyses. Earlier work was based on homogeneous material and discrete energy treatments, [5].

ii. The effect of blanket material choices in the overall neutron transport behaviour and subsequently in the transmutation of the armour material; in particular, a new PPCS plant model has been studied which had not been previously analysed.

This document describes these calculations and reports the main results and conclusions drawn from this study.

2. Tungsten transmutation and resonance self-shielding

Natural tungsten is made of five stable isotopes: ^{180}W (0.13%), ^{182}W (26.3%), ^{183}W (14.3%), ^{184}W (30.7%) and ^{186}W (28.6%). Under typical fusion neutron spectra, the bulk of the transmutation products arise from (n,γ) and (n,2n) reactions, and lead mainly to rhenium and osmium isotopes. The main pathways for their generation are:

$$^{186}\mathrm{W}(n,\gamma)^{187}\mathrm{W} \rightarrow (\beta\text{-})\ ^{187}\mathrm{Re} \quad \begin{cases} (n,\gamma)^{188m}\mathrm{Re} \rightarrow (\gamma)\ ^{188}\mathrm{Re} \rightarrow (\beta)\ ^{188}\mathrm{Os} \\ (n,2n)\ ^{186}\mathrm{Re} \rightarrow (\beta\text{-})\ ^{186}\mathrm{Os} \end{cases}$$

$$^{184}\mathrm{W}(n,\gamma)^{185}\mathrm{W} \rightarrow (\beta\text{-})\ ^{185}\mathrm{Re}(n,\gamma)^{186}\mathrm{Re} \rightarrow (\beta\text{-})\ ^{186}\mathrm{Os}$$

which are also sketched in Figure 1. Neutron absorption in ^{180}W generates traces of tantalum through β^+ decay of ^{181}W. The relative importance of these pathways is strongly dependent on the neutron spectra and therefore on the surrounding materials. In the energy range from1 eV to 10 keV the neutron absorption cross-sections of ^{184}W and ^{186}W present typical resonances, as can be seen in Figure 2. These arise when the energy of the incident neutron equals an excitation energy of the compound nucleus, and strong coupling of the wave functions occurs. The ^{186}W(n,γ)^{187}W cross-section presents a so-called *giant* resonance at ~20 eV. Outside the resonance region, neutron flux tends to follow smoothly the 1/*v* slowing-down, scattering and absorption laws. But at the resonace edge the sharp increase of the cross-section induces a decrease in the flux of roughly inverse proportion. The neutron flux has then two components: a smooth slowing-down function and a fine structure presenting sharp, localised flux depressions at resonance edges. These "dips" lead to a substantially reduced absorption reaction rate. This effect is called *self-shielding*, and is illustrated in Figure 3 comparing the neutron spectra calculated during the PPCS study for the non-armoured first wall (FW) of one of the plant models, with the result obtained when including a 2 mm tungsten armour. Only the latter presents a dip at the energy of the giant ^{186}W resonance.

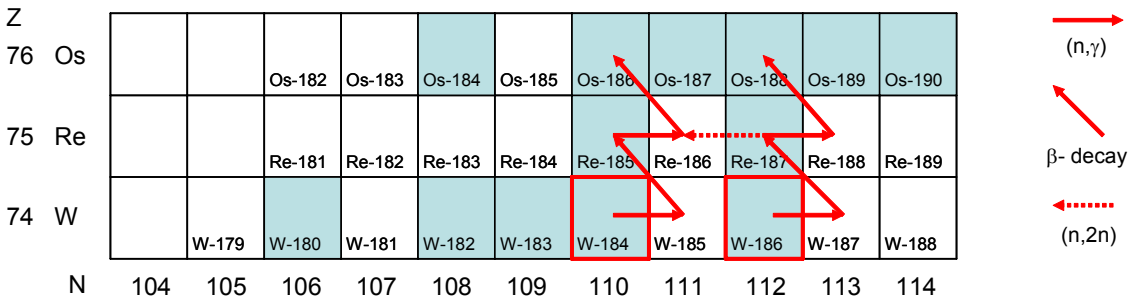

Fig. 1: Re and Os production pathways through tungsten neutron-induced transmutation. Stable isotopes are shaded.

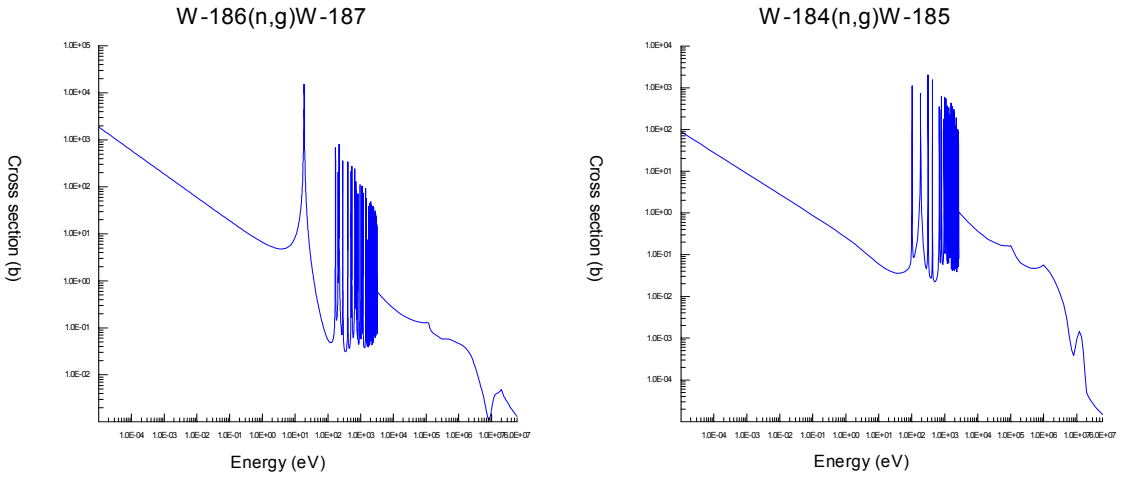

Fig. 2: European Activation File (EAF-2003) cross-section data for the $^{186}W(n,\gamma)^{187}W$, left, and $^{184}W(n,\gamma)^{185}W$ reactions, right.

The magnitude of this effect is very dependent on geometry, isotopes and surrounding materials. Previous studies pointed out its importance in tungsten isotopes under fusion neutron conditions, [6,7], and the strong dependence of the resonance absorption rate on these and on the degree of homogeneisation of the materials in the computational models used for the calculation of transmutation inventories.

The conclusion of this work was that the best solution for an accurate estimation of reaction rates, and the approach taken in this study, is to use heterogeneous representation of the materials with large resonance cross-sections along with pointwise, continuous-energy sampling of the reaction rate during the neutron transport calculations, rather than the multigroup treatment of inventory codes. This is so because

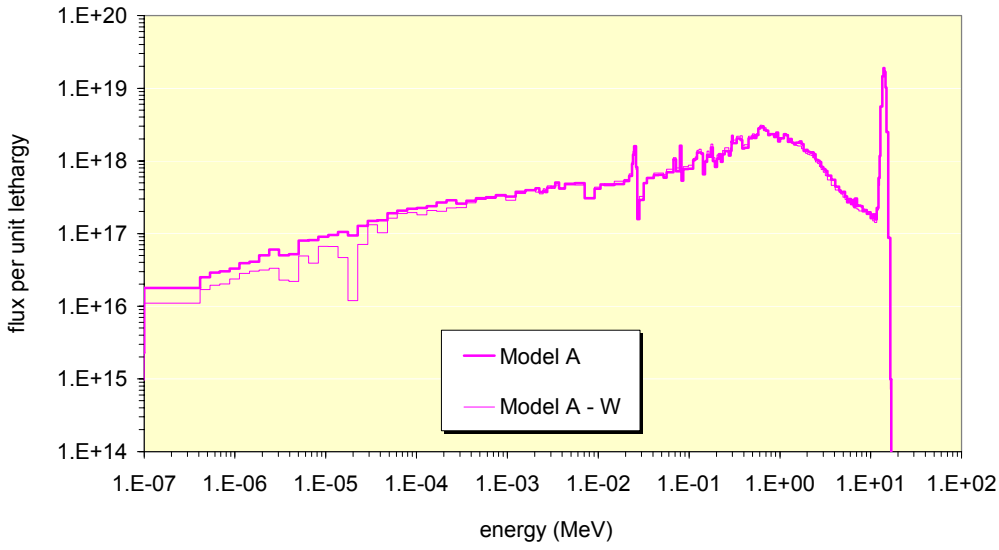

Fig. 3: Neutron spectra at the outboard midplane first wall of plant model A of the PPCS, based on a water-cooled liquid LiPb blanket concept, with (thin line) and without (thick line) tungsten armour.

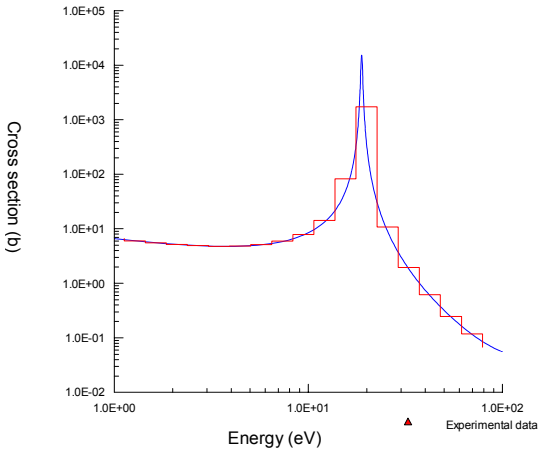

Fig. 4: Comparison between pointwise (continuous blue curve) and multigroup, fusion weighted EAF-2003 data (red histogram) of the $^{186}W(n,\gamma)^{187}W$ cross-section at the giant resonance region. The intrinsic error in transmutation calculations using inventory codes that rely on multigroup data, and result in overestimation of the reaction rate, is particularly magnified in giant resonances such as this one.

group averaging involves weighting using functions describing typical spectra, and an intrinsic error in the transmutation calculations using inventory codes relying on multigroup cross-section data is introduced, as the real spectra always differ from the functions used in the weighting and varies significantly within the bounds of a single energy group in the vicinity of resonances. This effect is particularly important in giant resonances, as illustrated in Figure 4, where serious over-prediction of the reaction rate may result. For these reasons, Monte Carlo methods combining versatile, continuous geometry and material modelling and continuous energy treatment are preferred, enabling accurate calculation of reaction rates. The MCNP code, using cross-section data based on the ENDF/B VI evaluated libraries, was chosen for the calculations reported here.

Therefore, the methodology involves obtaining reaction rates of $^{186}W(n,\gamma)^{187}W$ directly in MCNP using continuous treatment, and then feeding an artificial *effective cross-section* to the inventory code, σ_{eff}, overriding the multigroup library value. This effective cross-section is calculated from MCNP data following Equation 1, where RR_{mcnp} and ϕ_{mcnp} are the reaction rate and neutron flux calculated by the code, respectively, and N is the number density of ^{186}W atoms:

$$\sigma_{eff} = \frac{RR_{mcnp}}{N\phi_{mcnp}} \qquad (1)$$

Previous PPCS work accounting for a 2 mm tungsten armour coating the FW of plant models A and B, [2], provides a first estimation of the importance of heterogeneous treatment. Inventory code results show effective cross-section values of the $^{186}W(n,\gamma)^{187}W$ reaction being a factor of up to 6 lower than for the homogeneous case in [5], as shown in Table 1; tungsten transmutation product levels are consequently reduced. The difference between the continuous and multigroup treatments then was found to be a factor of up to ~3.

Table 1: EAF and MCNP σ_{eff} results of earlier work (in barns).

	EAF discrete treatment		MCNP continuous treatment
	ref. [5]	ref. [2]	ref. [2]
PMA	5.77	1.08	0.40
PMB	7.51	1.23	0.40

3. Material choices and neutron behaviour: the PPCS plant models

In plasma-facing layers, usually much thinner than the average mean free path, the neutron energy spectrum is dominated by unscattered 14.1 MeV neutrons for which (n,γ) reactions are relatively unimportant. Low energy neutrons, however, can be backscattered from outer structures at levels which may produce high reaction rates in the resonance region. The choice of materials in the surrounding blanket and divertor structures will strongly determine those levels, and is a crucial factor affecting reaction rates in thin layers of isotopes with giant resonances at low energies.

PPCS neutron transport analyses clearly illustrate this effect. Figure 5 shows a comparison of the neutron spectra in the tungsten amour of three of the five conceptual plant models in the study. These correspond to the so-called *near-term* models, whose plasma physics and technology assumptions are not far from present capabilities and therefore represent the earliest options available for future power production using magnetically confined burning plasmas. The blanket concepts of these three models have been developed from proposals for the European ITER Test Blanket Module

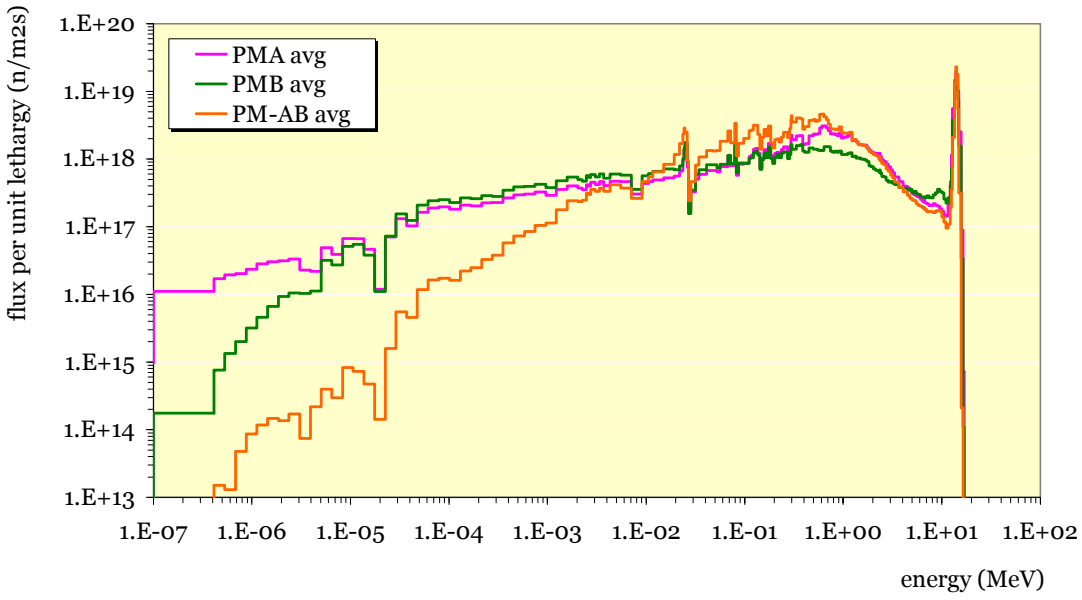

Fig. 5: Histograms of neutron energy spectra at the outboard midplane armour of plant model A, B and AB of the PPCS, showing the giant ^{186}W (n,γ) resonance dip at ~20 eV.

Table 2: PPCS plant model main features and materials.

	PMA	PMB	PM-AB
Electrical power output (GW)	1.55	1.33	1.50
Fusion power (GW)	5.00	3.60	4.24
Major radius (m)	9.55	8.60	9.56
Average neutron wall load (MW/m^2)	2.2	2.0	1.9
Divertor peak heat load (MW/m^2)	15	10	10
Blanket:			
Structural material	Eurofer	Eurofer	Eurofer
Breeder / neutron multiplier	LiPb	Li_4SiO_4/Be	LiPb
Armour	W	W	W
Coolant	H_2O	He	He
Divertor:			
Structural material	Eurofer	Eurofer	Eurofer
Heat sink material	Cu and W alloys	W alloy	W alloy
Plate	W	W	W
Coolant	H_2O	He	He

programme. Plant model A (PMA) is based on a water-cooled, liquid LiPb blanket concept, and also on a water cooled divertor concept using copper alloy heat sinks. The other two are entirely helium cooled: plant model B (PMB) blanket concept uses lithium orthosilicate (Li_4SiO_4) and beryllium pebble beds for tritium production, whereas plant model AB (PM-AB) uses LiPb again. All models in the PPCS study were optimised to achieve tritium self-sufficiency and deliver similar electrical output while minimising the cost of electricity. The main material choices and plant parameters are summarised in Table 2.

The presence of moderating materials such as water and beryllium in models A and B is clearly noticeable in the armour neutron spectra: both show low energy flux levels more than one order of magnitude higher than model AB, which lacks any of these materials. Model A spectrum shows enhanced moderation with neutron flux about two orders of magnitude higher than model B at very low energy, due to scattering in hydrogen atoms in the water. Model AB non-moderated spectra is also representative of the other two concepts in the PPCS, models C and D based on *advanced* fusion scenarios, because the blanket and divertor designs are based on similar materials and present similar lay-outs. Consequently these three spectra, and the power plant concepts they represent, are characteristic of the neutron behaviour of the whole range of fusion power plant options spanned in the PPCS. In order to asses the importance of material selection and blanket/divertor designs in the transmutation of tungsten PF layers, it was decided to perform calculations for these three models. Information on plant dimensions, geometry, plasma neutron source, materials and radial build was obtained from PPCS literature, [8].

4. Computational modelling

The HERCULES system, [9], assisted in the generation of the geometry and input files for the neutron transport and activation calculations, performed using the MCNP, [10], and FISPACT, [11], codes. The three PPCS selected concepts were modelled within the constraints of this system, which approximates the tokamak geometry into a toroidally symmetric model whose poloidal cross section is parametrically defined following the ultimate plasma contour, and is divided into radial layers and poloidal sectors. One sector within a layer defines a cell, and each cell is filled with a mixture of materials matching the design as closely as possible. The divertor is coarsely approximated by assigning different material mixtures to a user-specified number of poloidal sectors located at the bottom of the machine, below the plasma. Figures 6 and 7 and Table 3 show example poloidal sections of the models, details of the outboard midplane and divertor target plates PF regions, and material specifications of the different layers. All three had heterogeneous tungsten PF layers, the radial detail of these increased in order to study the penetration of low energy neutrons backscattered from outer structures and into the tungsten.

Table 3: Details of geometry and material specifications at the first wall and divertor plates regions of the three PPCS models in the study.

region	plant model	layer no.	thickness (mm)	component	material composition
first wall	PMA	1-5	0.4	armour	tungsten
		6	10	first wall	Eurofer + water
		7	11	first wall	Eurofer
		8	~850	breeder zone	Eurofer + $Li_{17}Pb_{83}$ + water
	PMB	1-5	0.4	armour	tungsten
		6	18	first wall	Eurofer + He
		7	5	first wall	Eurofer
		8	~500	breeder zone	Eurofer+Be+ Li_4SiO_4+He
	PM-AB	1-5	0.4	armour	tungsten
		6	15	first wall	Eurofer + He
		7	10	first wall	Eurofer + He
		8	~700	breeder zone	Eurofer + $Li_{17}Pb_{83}$ + He
divertor	PMA	1-5	0.4	plates	tungsten
		6	10	heat sink	Eurofer + tungsten + CuCrZr + OFHCu + water
		7	11	heat sink	
		8	~850	structure	Eurofer + water
	PMB	1-5	0.4	plates	tungsten
		6	18	heat sink	Eurofer + tungsten + He
		7	5	heat sink	
		8	~500	structure	Eurofer + He
	PM-AB	1-5	0.4	plates	tungsten
		6	15	heat sink	Eurofer + tungsten + He
		7	10	heat sink	
		8	~700	structure	Eurofer + He

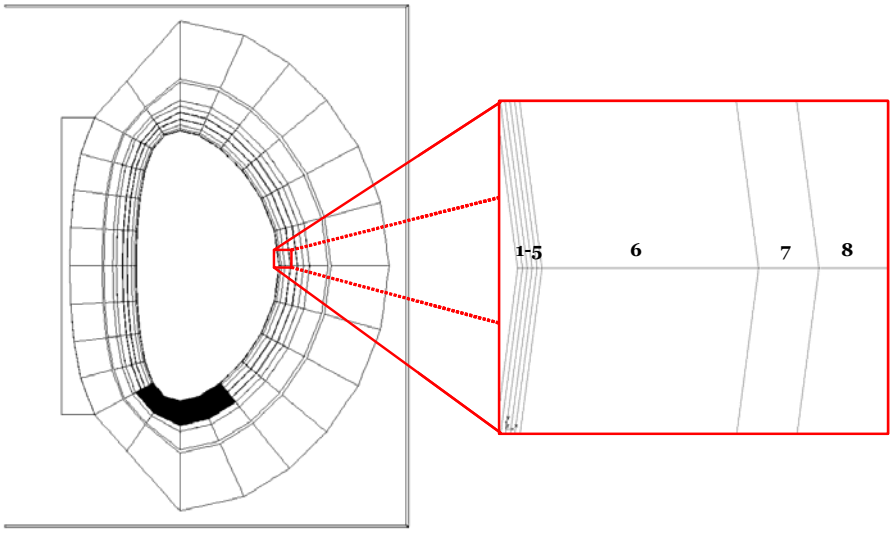

Fig. 6: Poloidal cross section and detail of the outboard midplane radial layering of the models developed with the HERCULES system.

Table 4 shows the elemental compositions of the most important materials present in the radial build of the models, as supplied to HERCULES. Natural isotopic abundance was assumed throughout except for the lithium in the breeder, assumed to be enriched in ^{6}Li up to 90% for LiPb, and up to 30% for lithium orthosilicate, according to design values. The plasma neutron source in the MCNP models was a typical fusion plasma source, represented using the parameters listed in Table 5. The shape is elliptical-triangular, and it assumes magnetic flux surfaces are surfaces of constant neutron emission. The energy distribution is gaussian (centred at 14.1 MeV and width governed by the core ion temperature), and the directional distribution is isotropic.

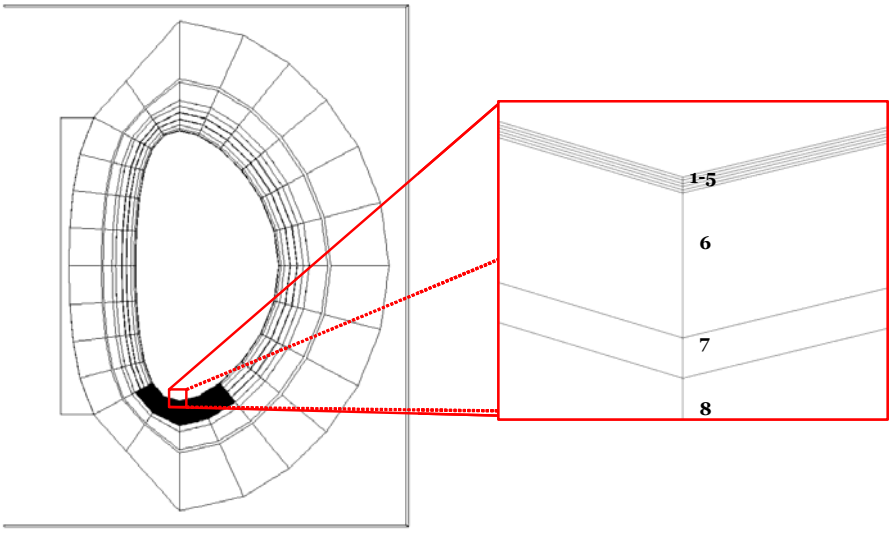

Fig. 7: Poloidal cross section and detail of the divertor plates radial layering of the models developed with the HERCULES system.

Table 4: Elemental compositions of the most important materials in the PPCS models (%wt).

	Eurofer	Be	LiPb	Li4SiO4	Water	OFHCu	CuCrZr	W
H		0.01	0.01	0.01	11.19			0.01
HE		0.01	0.01	0.01				0.01
LI			0.68	22.4				
BE		99.4	0.01	0.01				
B			0.01	0.01				
C	0.11	0.055	0.01	0.01				0.06
N	0.03	0.01						
O	0.01	0.04	0.01	54.2	88.81			0.1
MG			0.01	0.011				
AL		0.0184	0.01	0.052				
SI	0.05	0.0258	0.01	23.1				0.01
P			0.01	0.01				0.01
S			0.01	0.065				0.01
AR								0.01
CA				0.018				
TI	0.01		0.01					0.01
V	0.2	0.05	0.0986	0.01				0.01
CR	9		0.01				1	0.01
MN	0.4							
FE	88.949	0.0617		0.028				
NI		0.0106						
CU						100	98.9	
ZR			0.01	0.073			0.1	
CD				0.01				
IN								
SN		0.03		0.01				
TA	0.07							
W	1.1	0.01	0.01	0.01				99.4
PB			98.7	0.01				

5. Neutron transport results

Models generated with HERCULES were used in MCNP 4C3 on a parallel cluster of 71 dual processors running Linux. For efficiency of the computation an importance cell map was implemented (splitting plus Russian roulette); no other variance reduction techniques were employed. ENDF-VI nuclear data tables were used. Neutron energy spectra and $^{186}W(n,\gamma)^{187}W$ reaction rates were calculated in all cells of interest using track length estimation of the particle flux, and binned following the Vitamin-J multigroup scheme.

Table 5: Plasma parameters

Parameter	PMA	PMB	PM-AB
Major radius (m)	9.55	8.60	9.56
Aspect ratio	3.0	3.0	3.0
Core ion temperature (keV)	58.0	50.0	53.8
Elongation	1.7	1.7	1.7
Triangularity	0.27	0.27	0.27
Plasma peaking factor	1.7	1.7	1.7

5.1 First wall armour

Comparison of neutron spectra results in flux per unit lethargy at the outboard midplane armour of the three PPCS models was shown in Figure 4. Figure 8 shows a detail of the low energy range of the spectrum at different radial locations of PMA armour, namely the front and rear surfaces, compared with the same average. The dip in the resonance region is shallow at the rear interface with the blanket from where low energy neutrons are backscattered, populating this region, and deepens as it penetrates into the armour due to absorption in the giant resonance. The same effect is obtained in all three models, but it is significantly less important in model AB due to the poor moderation in the blanket.

Reaction rate results for $^{186}W(n,\gamma)^{187}W$ mirror this trend: they are summarised in Figure 9, showing a comparison of the radial variation of the effective cross-section results as calculated following Equation 1. The average value for PMA and PMB from [2] is also shown; calculations in this work had no spatial discretisation, thus correspond to the effective cross-section averaged over the 2 mm PMA and PMB armours, the difference between the two being in the third significant figure. Backscattered low energy neutrons from the blanket in PMA and PMB produce enhanced σ_{eff} values in the armour, and particularly so at the rear interface with the blanket where they are a factor of 3 greater than the average. The low energy neutron influx from the blanket seems to be promptly shielded by absorption in the giant resonance, in a matter of half a millimetre. Nothing of the sort is observed in PM-AB. Given the very similar shape of the spectra in the energy range of this resonance, it is likely that the difference between the results for models A and B at the interface with the blanket be due to absorption at lower energies, and to the enhanced moderation of the water coolant blanket concept.

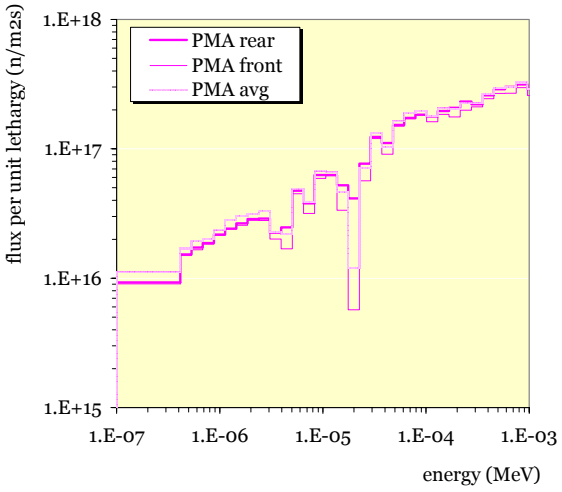

Fig. 8: Detail of low energy neutron spectra at different radial positions of the outboard midplane armour of plant model A.

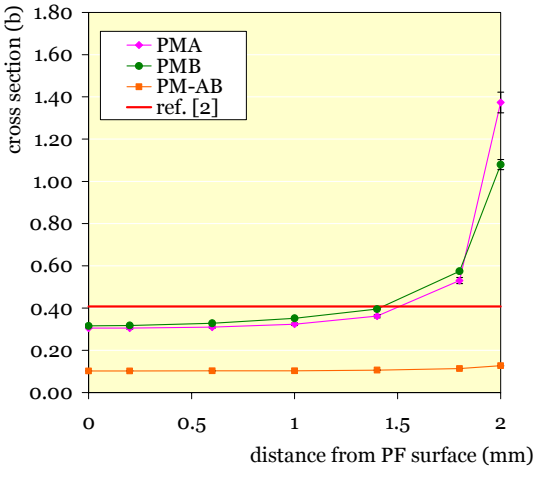

Fig. 9: $^{186}W(n,\gamma)^{187}W$ effective cross-section vs. radial distance from the PF surface at the outboard midplane of the three PPCS models.

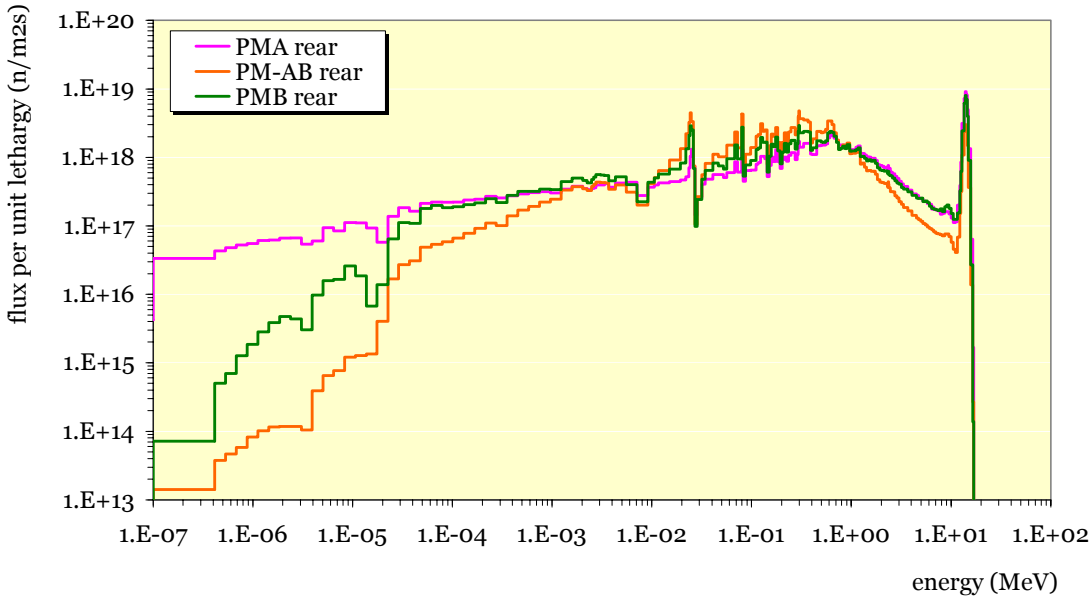

Fig. 10: Histograms of neutron energy spectra at the rear of the divertor PF region of plant models A, B and AB of the PPCS, showing the giant ^{186}W (n,γ) resonance dip at ~20 eV.

5.2 Divertor

Neutron transport results at the front of the divertor target plate region are very similar to those obtained at the front of the outboard midplane armour, for the three models. At the rear of the divertor, however, the situation is significantly different; neutron spectra are compared in Figure 10.

The only divertor that reproduces the outboard midplane trends is PMA, due to the water cooling of this structure producing similar moderation and backscatter of low energy neutrons, enhanced reaction rates in the interface with the PF layer, and shielding of these neutrons by the giant resonance as they penetrate this layer. This can

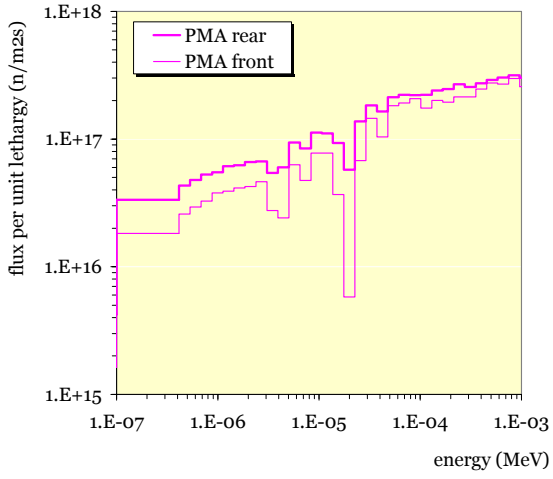

Fig. 11: Detail of low energy neutron spectra at different radial positions of the divertor of plant model A.

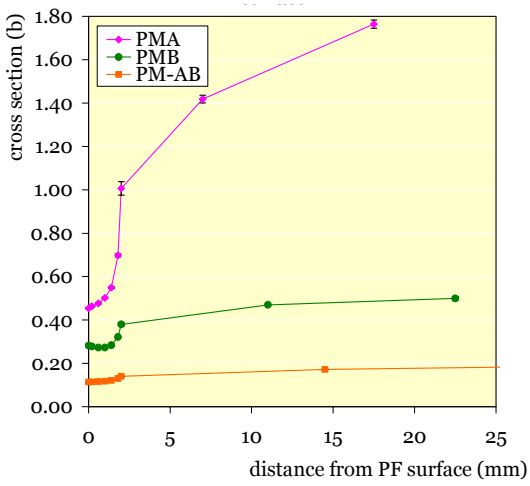

Fig. 12: ^{186}W(n,γ)^{187}W effective cross-section vs. radial distance from the PF surface in the divertor region of the three PPCS models.

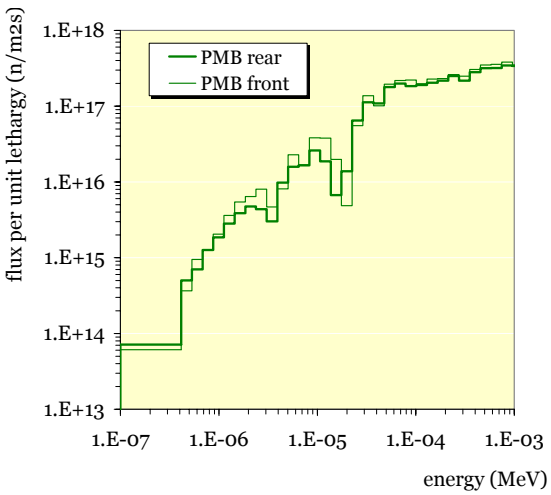

Fig. 13: Detail of low energy neutron spectra at different radial positions of the divertor of plant model B.

be seen in Figures 11 and 12. In PMB and PM-AB, however, the lack of moderating material (water/beryllium) in the divertor results in no enhanced amounts of low energy neutrons at the interface or at the plates at all. Resonance shielding is still noticeable but less pronounced than in model A. Detail of the low energy range of the spectrum at different radial locations of PMB divertor, namely the front and rear surfaces, is shown in Figure 13. PMB reaction rates are still higher than those of PM-AB due to the generally higher low energy and thermal neutron flux: a reminiscence of moderation in the far away blanket.

The combined use of importance maps and parallel computing provided good statistics while optimising time and computer resources in these Monte Carlo calculations. Only a small fraction of tally errors on individual energy bins were greater than 10%. The code's statistical checks provided further confidence in the validity of the results.

6. Transmutation analysis

Transmutation calculations were performed using neutron spectra obtained from the previously described calculations in the inventory code FISPACT and EAF discrete data libraries (2003 versions), [12]. Pure tungsten, in its natural abundance isotopic composition, was assumed to be the original material. Irradiation histories ran up to 10 years of continuous irradiation – a period covering the entire service life of the components. Appropriate commands were used in order to override the $^{186}W(n,\gamma)^{187}W$ EAF cross-section data in the EAF libraries and substitute them with σ_{eff} values calculated from MCNP results. A comparison between the two is shown in Figure 14.

The overestimation of the reaction rate in the armour due to the multigroup treatment can be seen more clearly in Figure 15, where the variation with distance of the ratio between σ_{eff} values and those calculated by FISPACT using multigroup data is shown. Results are in agreement with earlier work, [2, 6]. The intrinsic error introduced during the weighting process is clearly observed in this Figure: the more similar the neutron spectrum is to the functions used in the weighting, the closer the ratio between the two cross-section values is to unity.

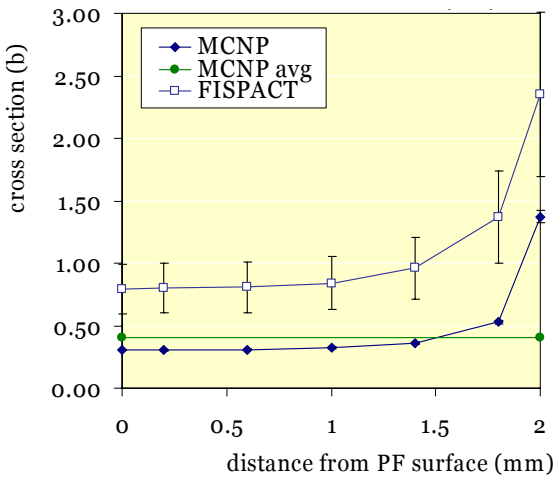

Fig.14: Comparison between effective cross-section values calculated with MCNP results and by the FISPACT code, at PMA outboard midplane.

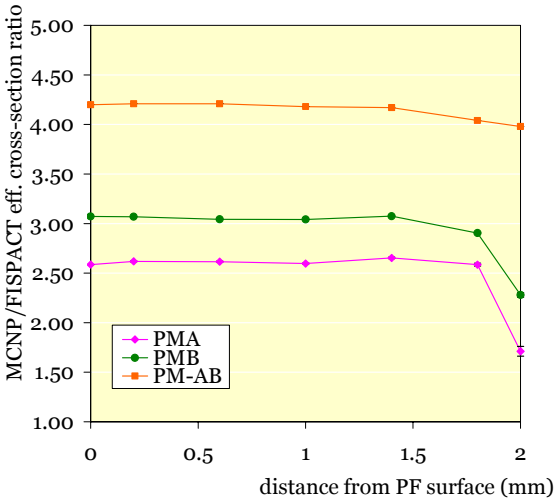

Fig. 15: Variation with distance of the ratio between continuous MCNP and discrete FISPACT σ_{eff} results.

Time histories of Re and Os levels were produced and delivered to pertinent experts for the analysis of potential for σ and χ phase formation, [13]. Preliminary judgements show that in no case the σ field of the thermodynamic phase diagram is reached within the service lifetime of the armour or divertor plates. Further investigation of the potential formation of χ phase is needed. Examples of those time histories at worst-case locations, where σ_{eff} and reaction rates are highest (i.e. rear of the armour and plates), are shown in Figures 16 and 17. Table 6 is a summary of the W, Re and Os levels at different significant irradiation times.

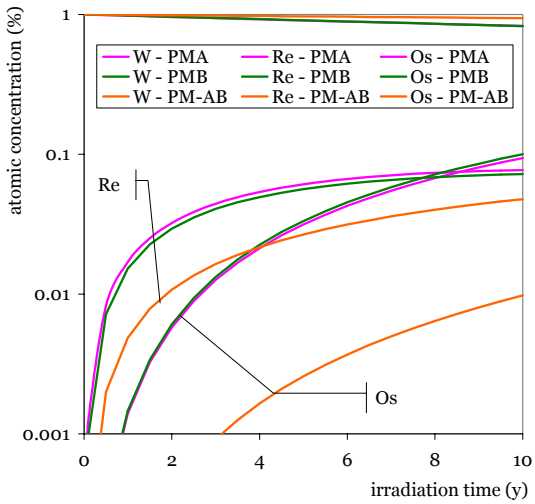

Fig.16: Time variation of W, Re and Os concentrations at the outboard midplane interface between the armour and blanket of the three PPCS models.

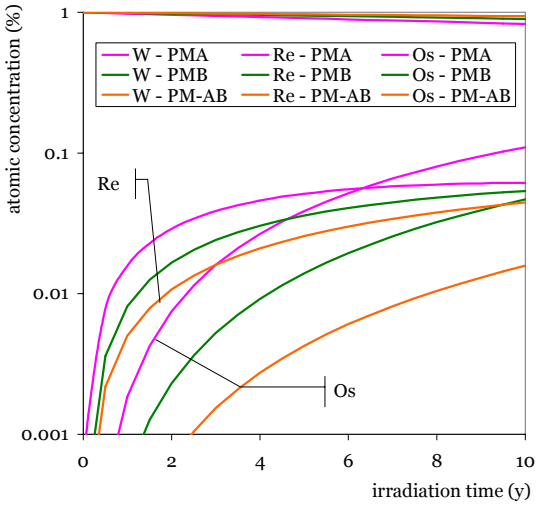

Fig.17: Time variation of the W, Re and Os concentrations at the rear of the divertor target plate region of the three PPCS plant models.

Table 6: Summary of W/Re/Os levels at different irradiation times.

armour	time (y)	W (%at)	Re (%at)	Os (%at)	divertor	time (y)	W (%at)	Re (%at)	Os (%at)
PMA									
front	2.5	97.70	1.82	0.46	front	2.5	97.80	1.69	0.51
	5	95.30	3.01	1.69		5	95.50	2.71	1.83
	10	90.60	4.11	5.24		10	90.80	3.63	5.55
rear	2.5	95.20	3.86	0.89	rear	2.5	95.40	3.42	1.15
	5	90.70	6.10	3.15		5	91.00	5.13	3.87
	10	82.90	7.71	9.38		10	82.80	6.15	11.00
PMB									
front	2.5	97.40	2.11	0.51	front	2.5	97.90	1.78	0.35
	5	94.50	3.54	1.93		5	95.50	3.09	1.36
	10	89.00	4.92	6.11		10	90.90	4.55	4.53
rear	2.5	95.50	3.54	0.94	rear	2.5	97.60	2.05	0.36
	5	91.00	5.63	3.33		5	95.00	3.59	1.40
	10	82.80	7.23	10.00		10	89.90	5.38	4.68
PM-AB									
front	2.5	98.60	1.30	0.06	front	2.5	98.80	1.13	0.06
	5	97.20	2.55	0.26		5	97.50	2.23	0.23
	10	94.50	4.59	0.90		10	95.10	4.02	0.88
rear	2.5	98.60	1.36	0.06	rear	2.5	98.60	1.34	0.10
	5	97.00	2.67	0.30		5	97.00	2.57	0.43
	10	94.20	4.78	0.96		10	94.00	4.45	1.58

7. Conclusions

Transmutation calculations using heterogeneous, continuous-energy treatment of the giant ^{186}W neutron absorption cross-section resonance have been performed, in order to account for self-shielding effects during the estimation of Re and Os levels in thin plasma-facing layers of tungsten irradiated in typical fusion power plant conditions. Three concepts in the European Power Plant Conceptual Study were chosen as representative of a whole range of options. Neutron transport analyses using Monte Carlo methods with continuous energy treatment provided effective cross-section data to be used in an inventory code which otherwise makes use of multigroup nuclear data libraries. Results allow confirmation and estimation of the influence in the self-shielding of the following factors: (i) the heterogeneous spatial treatment, (ii) the continuous energy treatment, and (iii) the influence of surrounding materials, which determine neutron behaviour in the plasma-facing layer.

Earlier work findings show that homogeneous treatment of the tungsten armour in plant models A and B artificially increases the effective ^{186}W(n,γ)^{187}W cross-section by a factor of up to 6. Discrete treatment effects observed here depend significantly on the neutron energy spectrum, and vary up to a factor of 4 for those being more different

from the weighting functions. These values are in agreement with earlier reports. In general terms, the presence of moderating materials such as water or beryllium in the blanket or divertor increases significantly tungsten transmutation rates in the plasma-facing layer, and dramatically so at the interface with the layer. This is due to backscattered low energy neutrons, but since those with the ^{186}W resonance energy are shielded within a few mean free paths (~0.5 mm) the effective cross-section decays equally promptly. This result gives rise to the concern that, if transmutation rates led to irradiation-induced embrittlement here, the integrity of the entire armour would be challenged by the failure of the interface with the blanket. However, in no case the calculated Re and Os levels seem able to trigger the formation of brittle σ phase in the W-Re-Os alloy during the service lifetime of the armour or divertor.

Acknowledgements

The author wishes to thank Dr GA Cottrell for his encouragement and guidance, and Dr NP Taylor for many valuable discussions. This work was funded jointly by the UK Engineering and Physical Sciences Research Council, and EURATOM.

References

[1] G Marbach, I Cook, D Maisonnier, *Fusion Engineering and Design* **63-64** (2002), 1-9.
[2] NP Taylor, R Pampin, to appear in *Fusion Engineering and Design* (Proc. 7th ISFNT conference, Tokyo, May 2005).
[3] Y Nemoto, A Hasegawa, M Satou, K Abe, *Journal of Nuclear Materials* **283-287** (2000), 1144.
[4] Y Nemoto, A Hasegawa, M Satou, K Abe, Y Hiraoka, *Journal of Nuclear Materials* **324** (2004), 62.
[5] GA Cottrell, *Journal of Nuclear Materials* **334** (2004), 166.
[6] J-Ch Sublet, ME Sawan, *Fusion Engineering and Design* **45** (1999), 65-73.
[7] J-Ch Sublet, UKAEA Fusion report, UKAEA FUS 368, June 1997.
[8] D Maisonnier et al. for the PPCS team, Final report of the European PPCS study, EFDA-RP-RE-5.0, September 2004.
[9] R Pampin, PJ Karditsas, to appear in *Fusion Engineering and Design* (Proc. 7th ISFNT conference, Tokyo, May 2005).
[10] JF Briesmeister, Los Alamos National Laboratory report, LA-13709-M, 2000.
[11] RA Forrest, UKAEA Fusion report, UKAEA FUS 485, January 2003.
[12] RA Forrest, J Kopecky and J-Ch Sublet, UKAEA Fusion report, UKAEA FUS 486, January 2003.
[13] GA Cottrell, EUROMAT'05 conference, Prague, September 2005.